

Why are ELEvoHI CME arrival predictions different if based on STEREO-A or STEREO-B heliospheric imager observations?

Juergen Hinterreiter¹, Tanja Amerstorfer¹, Martin Reiss¹, Christian Moestl², Manuela Temmer³, Maik Bauer¹, Ute V. Amerstorfer⁴, Rachel Louise Bailey⁵, Andreas J Weiss¹, Jackie A Davies⁶, Luke Barnard⁷, and Mathew J Owens⁷

¹Space Research Institute, Austrian Academy of Sciences

²Austrian Academy of Sciences

³Institute for Geophysics, Astrophysics and Meteorology, University of Graz, Universitätsplatz 5, A-8010 Graz, Austria

⁴Space Research Institute (ÖAW)

⁵Zentralanstalt für Meteorologie und Geodynamik

⁶Rutherford Appleton Laboratory

⁷University of Reading

November 26, 2022

Abstract

Accurate forecasting of the arrival time and arrival speed of coronal mass ejections (CMEs) is a unsolved problem in space weather research. In this study, a comparison of the predicted arrival times and speeds for each CME based, independently, on the inputs from the two STEREO vantage points is carried out. We perform hindcasts using ELLipse Evolution model based on Heliospheric Imager observations (ELEvoHI) ensemble modelling. An estimate of the ambient solar wind conditions is obtained by the Wang-Sheeley-Arge/Heliospheric Upwind eXtrapolation (WSA/HUX) model combination that serves as input to ELEvoHI. We carefully select 12 CMEs between February 2010 and July 2012 that show clear signatures in both STEREO-A and STEREO-B HI time-elongation maps, that propagate close to the ecliptic plane, and that have corresponding in situ signatures at Earth. We find a mean arrival time difference of 6.5 hrs between predictions from the two different viewpoints, which can reach up to 9.5 hrs for individual CMEs, while the mean arrival speed difference is 63 km s^{-1} . An ambient solar wind with a large speed variance leads to larger differences in the STEREO-A and STEREO-B CME arrival time predictions ($\sigma_{cc} = 0.92$). Additionally, we compare the predicted arrivals, from both spacecraft, to the actual in situ arrivals at Earth and find a mean absolute error of 7.5 ± 9.5 hrs for the arrival time and $87 \pm 111 \text{ km s}^{-1}$ for the arrival speed. There is no tendency for one spacecraft to provide more accurate arrival predictions than the other.

1 **Why are ELEvoHI CME arrival predictions different if**
2 **based on STEREO-A or STEREO-B heliospheric**
3 **imager observations?**

4 **Jürgen Hinterreiter^{1,2}, Tanja Amerstorfer¹, Martin A. Reiss^{1,3}, Christian**
5 **Möstl^{1,3}, Manuela Temmer², Maike Bauer^{1,2}, Ute V. Amerstorfer¹, Rachel L.**
6 **Bailey^{1,4}, Andreas J. Weiss^{1,2,3}, Jackie A. Davies⁵, Luke A. Barnard⁶, Mathew**
7 **J. Owens⁶**

8 ¹Space Research Institute, Austrian Academy of Sciences, Schmiedlstraße 6, 8042 Graz, Austria

9 ²University of Graz, Institute of Physics, Universitätsplatz 5, 8010 Graz, Austria

10 ³Institute of Geodesy, Graz University of Technology, Steyrergasse 30, 8010 Graz, Austria

11 ⁴Conrad Observatory, Zentralanstalt für Meteorologie und Geodynamik, Vienna, Austria

12 ⁵RAL Space, Rutherford Appleton Laboratory, Harwell Campus, Didcot OX11 0QX, UK

13 ⁶Department of Meteorology, University of Reading, Reading, UK

14 **Key Points:**

- 15 • A comparison of CME arrival time and speed predictions from two vantage
16 points was carried out using ELEvoHI
- 17 • A highly structured ambient solar wind flow leads to larger arrival time differ-
18 ences between STA and STB predictions
- 19 • The assumption of a rigid CME front in ELEvoHI and other HI-based methods
20 is most probably too simplistic

Corresponding author: Jürgen Hinterreiter, juergen.hinterreiter@oeaw.ac.at

Abstract

Accurate forecasting of the arrival time and arrival speed of coronal mass ejections (CMEs) is a unsolved problem in space weather research. In this study, a comparison of the predicted arrival times and speeds for each CME based, independently, on the inputs from the two STEREO vantage points is carried out. We perform hindcasts using ELLipse Evolution model based on Heliospheric Imager observations (ELEvoHI) ensemble modelling. An estimate of the ambient solar wind conditions is obtained by the Wang-Sheeley-Argé/Heliospheric Upwind eXtrapolation (WSA/HUX) model combination that serves as input to ELEvoHI. We carefully select 12 CMEs between February 2010 and July 2012 that show clear signatures in both STEREO-A and STEREO-B HI time-elongation maps, that propagate close to the ecliptic plane, and that have corresponding in situ signatures at Earth. We find a mean arrival time difference of 6.5 hrs between predictions from the two different viewpoints, which can reach up to 9.5 hrs for individual CMEs, while the mean arrival speed difference is 63 km s^{-1} . An ambient solar wind with a large speed variance leads to larger differences in the STEREO-A and STEREO-B CME arrival time predictions ($cc = 0.92$). Additionally, we compare the predicted arrivals, from both spacecraft, to the actual in situ arrivals at Earth and find a mean absolute error of 7.5 ± 9.5 hrs for the arrival time and $87 \pm 111 \text{ km s}^{-1}$ for the arrival speed. There is no tendency for one spacecraft to provide more accurate arrival predictions than the other.

1 Introduction

Understanding the dynamics of coronal mass ejections (CMEs) in the heliosphere is a key aspect of space weather research. CMEs are huge clouds of energetic and magnetized plasma (Hundhausen, Stanger, & Serbicki, 1994) erupting from the solar corona that may reach speeds of up to 3000 km s^{-1} . When they hit Earth, CMEs can produce strong geomagnetic storms (Gosling, Bame, McComas, & Phillips, 1990; Kilpua, Jian, Li, Luhmann, & Russell, 2012; Richardson & Cane, 2012; Srivastava & Venkatakrishnan, 2004) causing communication and navigation system problems, damaging satellites and can even cause power outages (Cannon, 2013). The need for accurate predictions of CMEs, both CME arrival time and speed, is becoming increasingly important (Owens, Lockwood, & Barnard, 2020), because humankind, more than ever, depends on advanced technology.

Shortly after their eruption, CMEs can be observed in coronagraph images. Two of the few space-borne coronagraphs in operation are the Large Angle and Spectrometric Coronagraph (LASCO) C2 and C3 on-board the Solar and Heliospheric Observatory (SoHO; Brueckner et al., 1995). SoHO is situated in a Lissajous orbit around Lagrange point 1 (L1), about 1.5 million km upstream of Earth in the Sun-Earth line.

The launch of the Solar Terrestrial Relations Observatory (STEREO; Kaiser et al., 2008) twin-spacecraft mission in 2006 provided an unprecedented opportunity to observe CMEs from off the Sun-Earth line. The two spacecraft orbit the Sun slightly closer (STEREO Ahead; STA) and slightly further (STEREO Behind; STB) than Earth, leading to a separation of each spacecraft by about 22° per year from Earth in opposite directions. Both spacecraft are equipped with the In-situ Measurements of Particles and CME Transients (IMPACT; Luhmann et al., 2008) instrument package to measure solar wind speed, density and magnetic field and additionally host a suite of imagers, such as the COR1 and COR2 (Howard et al., 2008) coronagraphs and the heliospheric imagers, HI1 and HI2 (Eyles et al., 2009). The wide-angle HI cameras provide observations of the heliosphere that allow us to track a CME from close to the Sun out to the orbit of Earth, particularly in the ecliptic plane.

CMEs are optically thin structures that expand rapidly, and decreasing density lowers the line-of-sight integrated intensity in white-light data. As a consequence,

72 the tracking of CME fronts and the interpretation of HI image data is difficult. Fur-
 73 thermore, the plane-of-sky assumption is not valid, and we must assume a certain
 74 longitudinal extent of the CME frontal shape.

75 CMEs may be influenced by different phenomena in the heliosphere, e.g. magnetic
 76 forces close to the Sun, high-speed solar wind streams, or by other CMEs (Kay &
 77 Opher, 2015; Lugaz et al., 2012; Möstl et al., 2015). The ambient solar wind can also
 78 affect the kinematic and morphological characteristics of CMEs (e.g. Gopalswamy et
 79 al., 2000; Gosling et al., 1990; Manoharan et al., 2004). A CME originating at a speed
 80 much faster than the ambient solar wind speed is likely to experience deceleration
 81 while slow CMEs may accelerate during their propagation (Manoharan & Mujiber
 82 Rahman, 2011; Richardson & Cane, 2010). Hence, not only the propagation direction
 83 but also the kinematics and shape of CMEs can be altered (e.g. Y. D. Liu et al.,
 84 2014; Rollett et al., 2014; Ruffenach et al., 2015; Savani, Owens, Rouillard, Forsyth, &
 85 Davies, 2010; Zuccarello et al., 2012). By tracking CMEs far out in the heliosphere, we
 86 get an understanding of their interaction with the ambient solar wind and co-rotating
 87 interaction regions.

88 Over the last decades, a vast number of CME prediction models have been de-
 89 veloped. They include empirical models, e.g. Effective Acceleration Model (EAM;
 90 Paouris & Mavromichalaki, 2017), which use relationships between observable param-
 91 eters and the transit time. There are also drag-based models, (e.g. DBM; Vršnak et
 92 al. 2013, DBEM; Dumbović et al. 2018, ANTEATR; Kay, Mays, and Verbeke 2020),
 93 that make use of physics-based equations and account for drag between the ambient
 94 solar wind and the CME. Other models make use of HI images, which require tech-
 95 niques to convert the measured elongation into radial distance. For example, the fixed
 96 phi fitting (FPF; Rouillard et al., 2008; Sheeley, Walters, Wang, & Howard, 1999)
 97 technique considers a CME as a single point, propagating at a constant speed, and
 98 provides an estimate of the constant direction of the CME propagation relative to the
 99 observer from the apparent acceleration within a sequence of HI images. The har-
 100 monic mean fitting (HMF; Lugaz, 2010; Möstl et al., 2011) method is similar except
 101 that it describes a CME as a circle that remains attached to the Sun-center. The
 102 self-similar-expansion fitting (SSEF; Davies et al., 2012; Lugaz et al., 2010; Möstl &
 103 Davies, 2013) technique describes a CME as a circle having an increasing radius as
 104 it propagates away from the Sun in such a way that it maintains a constant angular
 105 width. FPF and HMF are extremes of the SSEF technique with a half width of 0°
 106 and 90° , respectively. More sophisticated models combine both the drag-based ap-
 107 proach and HI observations (e.g. DBM fitting; Žic, Vršnak, and Temmer 2015, Ellipse
 108 Evolution model based on HI observations, ELEvoHI; Amerstorfer et al. 2018; Rollett
 109 et al. 2016). Finally, numerical models, which are computational heavy, solve mag-
 110 netohydrodynamic (MHD) equations (e.g., ENLIL; Odstrcil et al. 2004, EUHFORIA;
 111 Pomoell and Poedts 2018) simulating the ambient solar wind in the full heliosphere
 112 based on synoptic photospheric magnetic-field maps. CMEs are then injected into
 113 these models to provide predictions regarding the arrival time and arrival speed at
 114 different locations in the heliosphere.

115 As noted above, ELEvoHI aims to predict the arrival time and arrival speed of
 116 CMEs. The model assumes an elliptical shape for the CME front and incorporates the
 117 drag exerted by the ambient solar wind. Also, different sources of ambient solar wind
 118 speed (e.g. provided by numerical models) can serve as input to ELEvoHI (Amerstorfer
 119 et al., 2020). In its latest version, the model can be used with STEREO-A HI beacon
 120 mode data to provide near real-time CME arrival predictions.

121 This study assesses ELEvoHI to evaluate arrival time and speed predictions of
 122 past CMEs using STEREO HI science-quality data. We perform ELEvoHI ensemble
 123 predictions for 12 CMEs, where each CME is modeled using input data from STA
 124 and STB, separately. In an idealized case, in which a CME with an elliptical front

Table 1: List of selected CMEs. *ID* and *Date* correspond to the unique identifier and the time of the first appearance of the CME in HI1 imagery, from the HELCATS catalog, for STA and STB spacecraft. *ICMECAT ID* is the identifier of the interplanetary coronal mass ejection (ICME) from an updated version of the HELCATS ICMECAT (Möstl et al., 2017), *ICME date* is the start time of the detected ICME and v_{ICME} is the measured in situ arrival speed obtained from the HELCATS ICMECAT.

Nr.	ID STA	Date STA	ID STB	Date STB	ICMECAT ID	ICME date	v_{ICME} [km s ⁻¹]
1	HCME_A... 20100203_01	2010-02-03 14:49	HCME_B... 20100203_01	2010-02-03 20:49	ICME_Wind... NASA_20100207_01	2010-02-07 18:04 ^{b)}	406±2
2	HCME_A... 20100319_01	2010-03-19 22:09	HCME_B... 20100319_01	2010-03-19 20:09	ICME_Wind... MOESTL_20100323_01	2010-03-23 22:29 ^{c)}	292±12
3	HCME_A... 20100403_01	2010-04-03 12:09	HCME_B... 20100403_01	2010-04-03 12:09	ICME_Wind... NASA_20100405_01	2010-04-05 07:55 ^{a)}	734±18
4	HCME_A... 20100408_01	2010-04-08 06:49	HCME_B... 20100408_01	2010-04-08 07:29	ICME_Wind... NASA_20100411_01	2010-04-11 12:20 ^{a)}	432±17
5	HCME_A... 20100523_01	2010-05-23 22:09	HCME_B... 20100524_01	2010-05-24 00:09	ICME_Wind... NASA_20100528_01	2010-05-28 01:52 ^{a)}	370±10
6	HCME_A... 20101026_01	2010-10-26 15:29	HCME_B... 20101026_01	2010-10-26 16:10	ICME_Wind... MOESTL_20101030_01	2010-10-30 09:15 ^{b)}	380±9
7	HCME_A... 20110130_01	2011-01-30 20:09	HCME_B... 20110130_01	2011-01-30 18:49	ICME_Wind... MOESTL_20110204_01	2011-02-04 01:50 ^{a)}	375±9
8	HCME_A... 20110214_02	2011-02-14 22:49	HCME_B... 20110214_02	2011-02-14 22:09	ICME_Wind... MOESTL_20110218_01	2011-02-18 00:48 ^{a)}	493±25
9	HCME_A... 20110906_02	2011-09-06 23:29	HCME_B... 20110907_01	2011-09-07 03:29	ICME_Wind... MOESTL_20110909_01	2011-09-09 11:46 ^{a)}	417±20
10	HCME_A... 20120123_01	2012-01-23 04:49	HCME_B... 20120123_01	2012-01-23 05:29	ICME_Wind... MOESTL_20120124_01	2012-01-24 14:36 ^{a)}	613±36
11	HCME_A... 20120614_01	2012-06-14 16:09	HCME_B... 20120614_01	2012-06-14 16:09	ICME_Wind... MOESTL_20120616_01	2012-06-16 19:34 ^{a)}	489±29
12	HCME_A... 20120712_02	2012-07-12 18:49	HCME_B... 20120712_01	2012-07-12 18:09	ICME_Wind... MOESTL_20120714_01	2012-07-14 17:38 ^{a)}	615±37

^{a)} shock arrival time

^{b)} time of density enhancement

^{c)} time of the magnetic flux rope

125 propagates in an ambient solar wind that is constant in space and time, one would
 126 expect to get similar results for the arrival time and arrival speed from the two different
 127 vantage points. Instead of inferring the propagation directions of the events under
 128 study from HI images (e.g. FPF, SSEF), as was done by Amerstorfer et al. (2018),
 129 we make use of coronagraph images and perform Graduated Cylindrical Shell (GCS;
 130 A. Thernisien, Vourlidis, & Howard, 2009; A. F. R. Thernisien, Howard, & Vourlidis,
 131 2006) reconstruction for each CME based on multi-vantage point coronagraph data.
 132 Additionally, we apply a combination of the Wang-Sheeley-Argé (Argé, Odstrčil, Pizzo,
 133 & Mayer, 2003) and the Heliospheric Upwind eXtrapolation (Owens & Riley, 2017;
 134 Riley & Lionello, 2011) model (WSA/HUX model combination; Reiss et al., 2019, 2020)
 135 to get an estimate of the ambient solar wind conditions in the heliosphere through
 136 which the CME propagates. With the additional information about the propagation
 137 direction of the CME and the modeled ambient solar wind, ELEvoHI is more likely to
 138 give better arrival time and arrival speed predictions.

139 In Section 2, we describe our data selection process, including the data products,
 140 and list all of the studied CMEs. Section 3 deals with the ELEvoHI setup and how
 141 the input data required by the model is obtained. In Section 4, we present our results
 142 and give reasons for the difference in the model predictions based on STA and STB
 143 input data. The discussion and further implementations of the model are included in
 144 Section 5.

2 Data Preparation

We select a period between February 2010 and July 2012 during which the STEREO spacecraft had a separation angle from Earth of about 65° to 120° respectively, from which we study 12 CMEs. The HELCATS HICAT CME catalog lists about 700 entries over this time range (Harrison et al., 2018). However, our list is constrained to 12 events, since the CMEs have to:

- 1) be observed by HI on both STA and STB spacecraft (as listed in the HIJoinCAT; Barnes et al., 2020)
- 2) propagate close to the ecliptic plane,
- 3) have a corresponding in situ signature at Earth,
- 4) be able to be tracked unambiguously in time-elongation maps.

Table 1 contains the list of selected CMEs with their unique identifier and the time of their first observation in HI1 images (according to the HELCATS catalog Version 6). The interplanetary CME (ICME) times and speeds are taken from version 2.0 of the HELCATS ICMECAT catalog (Möstl et al., 2020, see also the links in the data section). The ICMECAT assimilates ICME catalogs from different spacecraft into one consistent list, and was first published in Möstl et al. (2017). The ICME date as observed by the Wind spacecraft is defined by the shock arrival time, or, if no shock is present, the start of a density enhancement in front of the magnetic flux rope (MFR). If neither is observed, the ICME start time is taken as the start time of the MFR. The corresponding ICME speed is the mean proton bulk speed of either the sheath region, the density enhancement ahead of the MFR, or the speed of the MFR itself. The spread in the speed over the given interval for each event is indicated in Table 1 by a standard deviation. For Table 1, some times in the ICMECAT were originally taken from the Wind ICME catalog (Nieves-Chinchilla et al., 2018), while other events that were not present in the Wind catalog were added by Möstl et al. (2020) to the HELCATS ICMECAT.

To run ELEvoHI, we make use of several data products. Most important are images from HI onboard STEREO. The HI instrument on each STEREO spacecraft consists of two white-light wide-angle imagers, HI1 and HI2. HI1 has a field-of-view (FOV) extending from 4° – 24° elongation (angle from Sun center) in the ecliptic and HI2 has an angular FOV extending from 18.8° – 88.8° elongation in the ecliptic. The nominal cadence of the HI1 and HI2 science data is 40 minutes and 120 minutes, respectively. The science image bin size is 70 arc sec for HI1 and 4 arc min for HI2. For the additional input parameters to ELEvoHI, we developed the Ecliptic cut Angles from GCS for ELEvoHI tool (EAGEL, see Section 3.1). EAGEL ideally uses coronagraph images from STEREO COR1/COR2 and from LASCO C2/C3 onboard SoHO, but images from at least two different viewpoints are required. The FOV of COR1 ranges from $1.4 - 4 R_\odot$ and COR2, from $2 - 15 R_\odot$, while C2 has a FOV of $1.5 - 6 R_\odot$ and C3, $3.7 - 30 R_\odot$ (all quoted in the plane-of-sky). The cadence of the coronagraph science images is about 15 minutes.

3 Methods

3.1 EAGEL (Ecliptic cut Angles from GCS for ELEvoHI)

In this section, we present a newly developed Interactive Data Language (IDLTM) tool called EAGEL (Ecliptic cut Angles from GCS for ELEvoHI). EAGEL allows the user to determine the propagation direction, ϕ , and the half width, λ , within the ecliptic plane, based on GCS reconstruction of a CME. To perform GCS reconstruction, coronagraph images from at least two vantage points (STEREO and/or LASCO) are required. EAGEL provides the routines to download the required coronagraph

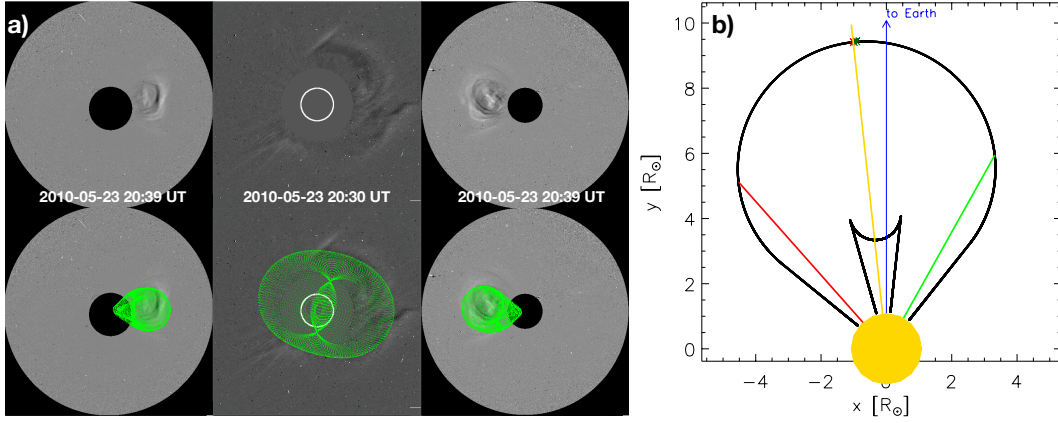


Figure 1: GCS reconstruction (left) and ecliptic cut of the wireframe (right) for event #5. a) Top row from left to right: STB/COR2, LASCO/C3, STA/COR2. Bottom row: same as top row but with the GCS wire frame overlaid. b) Ecliptic cut (black) of the GCS wire frame. Red and green lines show the boundaries selected by either EAGEL or the user. The yellow line defines the ecliptic propagation direction, ϕ , of the CME. The half angle, λ , is the angle between one boundary and ϕ . The blue arrow indicates the direction to Earth.

194 images, combines all the functions to perform GCS reconstruction, and produces a
 195 cut in the ecliptic plane. Standard pre-processing of the images is implemented in
 196 EAGEL to make the CME features clearly visible to the user, who can decide be-
 197 tween using background-subtracted, running-difference, and base-difference images.
 198 The user can then perform GCS reconstruction using the IDL SolarSoft procedure
 199 `rtscgcloud`. The top row of Figure 1a shows the coronagraph images (from left
 200 to right: STB/COR2, LASCO/C3, STA/COR2) for event #5. The bottom row ad-
 201 ditionally shows the GCS wire frame (green mesh). In its current version, ELEvoHI
 202 is a 2D prediction model giving results only in the ecliptic plane. Therefore, EAGEL
 203 calculates the ecliptic part of the GCS wire frame and selects the boundaries of the
 204 ecliptic cut (see red and green line in Figure 1b). The boundaries are defined to be
 205 the outermost points of each side of the ecliptic cut with respect to the apex direction
 206 from GCS reconstruction. This gives λ and ϕ , where the latter is defined to be exactly
 207 in between the two boundaries. A plot is shown to the user (Figure 1b) and, if needed,
 208 the boundaries can be changed manually. Once the user approves the selection, λ and
 209 ϕ relative to Earth and to the two STEREO spacecraft are stored and can be used by
 210 ELEvoHI.

211 In Table 2, we list the time (Date) of the STEREO coronagraph images used
 212 to get λ and ϕ for each event. EAGEL then selects the SoHO coronagraph images
 213 closest in time to the quoted date. The table further contains the GCS parameters
 214 (Lon , Lat , TA , AR , HA), λ , and the CME ecliptic propagation angle, ϕ , relative to
 215 Earth (ϕ_{Earth}) and relative to the two STEREO spacecraft (ϕ_{STA} and ϕ_{STB}) obtained
 216 from EAGEL. Lon is the longitude (here given in Stonyhurst coordinates) and Lat the
 217 latitude of the apex of the idealized hollow croissant shaped model. The tilt angle (TA)
 218 defines the tilt of the croissant and the half angle (HA) represents the angle between
 219 the center of the footpoints. The aspect ratio (AR) describes the spatial extent of the
 220 croissant.

221 When comparing Lon (longitude from GCS reconstruction) and ϕ_{Earth} (longitude
 222 relative to Earth from the ecliptic cut), it can be seen that the propagation direction

Table 2: GCS parameter obtained from fitting the hollow croissant shape the STEREO and SoHO coronagraph images. *Date*: time set in EAGEL to perform the reconstruction, *Lon*: GCS longitude (Stonyhurst coordinates), *Lat*: GCS latitude, *TA*: GCS tilt angle, *AR*: GCS aspect ratio, *HA*: GCS half angle, λ : half angle of the CME from the ecliptic cut, ϕ_{Earth} , ϕ_{STA} , ϕ_{STB} : propagation direction based on the ecliptic cut with respect to Earth, STA, STB, respectively.

Nr.	Date	Lon [°]	Lat [°]	TA [°]	AR	HA [°]	λ [°]	ϕ_{Earth} [°]	ϕ_{STA} [°]	ϕ_{STB} [°]
1	2010-02-03 15:54	355	-17	-1	0.33	30	36	-4	67	68
2	2010-03-19 17:39	23	-12	-7	0.29	19	30	22	44	93
3	2010-04-03 12:39	7	-19	15	0.39	30	38	9	58	81
4	2010-04-08 06:39	1	-10	-20	0.28	30	31	-2	70	69
5	2010-05-23 20:39	6	2	-15	0.48	18	35	-6	65	76
6	2010-10-26 14:39	18	-35	-28	0.51	30	18	-11	95	69
7	2011-01-30 21:24	351	-18	-20	0.33	12	24	-11	97	82
8	2011-02-15 04:08	10	-10	27	0.87	29	49	10	77	104
9	2011-09-06 23:39	29	20	-90	0.49	30	26	29	74	124
10	2012-01-23 04:39	19	41	64	0.77	55	37	9	99	123
11	2012-06-14 14:54	360	-28	11	0.90	30	53	1	116	117
12	2012-07-12 17:54	8	-12	68	0.46	30	26	14	106	129

223 obtained from the ecliptic cut is quite comparable to (within 5° of) the propagation
 224 direction from the GCS reconstruction. Only for CMEs #6 and #10 do we find a
 225 larger difference of close to 30° and 10°, respectively. The reason can be found in the
 226 combination of low/high latitude and large tilt angle. Therefore, the part within the
 227 ecliptic plane does not correspond well to the main propagation direction resulting
 228 from GCS reconstruction for these two CMEs.

229 3.2 WSA/HUX model

230 In the following paragraph, we summarize the main characteristics of the numerical
 231 framework used here for modelling the physical conditions in the evolving ambient
 232 solar wind flow. For this study, we make use of the framework shown in Reiss et al.
 233 (2019, 2020), but the components of this framework were developed by Wang and
 234 Sheeley (1995), Arge et al. (2003), Riley and Lionello (2011), and Owens and Riley
 235 (2017). Specifically, we use magnetic maps of the photospheric field from Global Os-
 236 cillation Network Group (GONG) provided by the National Solar Observatory (NSO)
 237 as input to magnetic models of the solar corona. Using the Potential Field Source
 238 Surface model (PFSS; Altschuler & Newkirk, 1969; Schatten, Wilcox, & Ness, 1969)
 239 and the Schatten current sheet model (SCS; Schatten, 1971) we compute the global
 240 coronal magnetic field topology. While the PFSS model attempts to find the potential
 241 magnetic field solution in the corona with an outer boundary condition that the field
 242 is radial at the source surface at 2.5 R_{\odot} , the SCS model in the region between 2.5 and
 243 5 R_{\odot} accounts for the latitudinal invariance of the radial magnetic field as observed by
 244 Ulysses (Wang & Sheeley, 1995). From the global magnetic field topology, we calcu-
 245 late the solar wind conditions near the Sun using the established Wang-Sheeley-Arge
 246 (WSA) model. To map the solar wind solutions from near the Sun to Earth, we use the
 247 Heliospheric Upwind eXtrapolation model (HUX) which simplifies the fluid momen-
 248 tum equation as much as possible. The HUX model solutions match the dynamical
 249 evolution explored by global heliospheric MHD codes fairly well while having low pro-
 250 cessor requirements. An example of the ambient solar wind modeled by WSA/HUX
 251 combination is shown in Figure 2.

252

3.3 ELEvoHI ensemble modeling

253

254

255

256

257

258

259

260

261

262

263

264

ELEvoHI uses HI time-elongation profiles of CME fronts and assumes an elliptical shape for those fronts to derive their interplanetary kinematics (detailed information about the underlying Ellipse Conversion method can be found in Rollett et al., 2016). The tracking of each CME was done manually using ecliptic time-elongation maps (j-maps; Davies et al., 2009; Sheeley et al., 1999), generated by extracting ecliptic data from STA and STB HI images. Transients, like CMEs, appear as a bright feature in the j-maps. To extract the time-elongation profiles, we use the SATPLOT tool implemented in IDLTM SolarSoft. It allows any user to measure the elongation, which is defined as the angle between the Sun - observer (STA or STB) line and the CME front. ELEvoHI converts the resulting time-elongation profiles to time-distance profiles, assuming an elliptical frontal shape using the ELEvoHI built-in procedure ELipse Conversion (ELCon; Rollett et al., 2016).

265

266

267

268

269

270

271

272

273

274

275

276

277

278

279

280

281

282

283

284

ELEvoHI accounts for the effect of the drag force exerted by the ambient solar wind, which is incorporated in the model. The drag force is an essential factor influencing the dynamic evolution of CMEs in the heliosphere. Within ELEvoHI, the time-distance track is fitted using a drag-based equation based on the drag-based model (DBM) given in Vršnak et al. (2013). The user has to define the start- and end point for the DBM fit (usually around 30 – 100 R_{\odot}) in the time-distance profile. In order to account for the de-/acceleration of the CME due to drag, an estimate of the ambient solar wind speed is needed. Here we make use of the WSA/HUX model (see Section 3.2). It provides the ambient solar wind conditions for a full Carrington rotation (see Figure 2). We only consider the part of the full map according to the start- and end-point selected by the user, and the CME propagation direction and half angle from EAGEL. From this area, surrounded by the white box in Figure 2, we take the median of the solar wind speed and define the uncertainties to be $\pm 100 \text{ km s}^{-1}$, based on a study by Reiss et al. (2020). They considered nine years (mid 2006 to mid 2015) and report a mean absolute error of the WSA solar wind speed prediction with respect to the in situ speed of 91 km s^{-1} . The obtained ambient solar wind speed with its uncertainty is split into steps of 25 km s^{-1} , which gives nine different input speeds to ELEvoHI. Based on these speeds, ELEvoHI selects the combination of drag parameter and ambient solar wind that best fits the time-distance profile for each ensemble member (for a detailed description see Rollett et al., 2016).

285

286

287

288

289

290

Since ELEvoHI is a 2D model, we are only interested in the propagation of a CME in the ecliptic plane. ϕ and λ , in this plane, are provided by EAGEL (see Section 3.1). The inverse ellipse aspect ratio, f , defines the shape of the assumed CME front in the ecliptic plane, where $f = 1$ represents a circular front while $f < 1$ corresponds to an elliptical CME front (with the semi-major axis perpendicular to the propagation direction)

291

292

293

294

295

296

297

298

299

300

301

302

303

304

To run ELEvoHI in ensemble mode, we vary ϕ , λ and f . A details description can be found in Amerstorfer et al. (2018) and the code is available online (see Section 6). ϕ and λ vary over a range of $\pm 10^\circ$ from their values obtained from EAGEL, with a step size of 2° and 5° , respectively. This range is defined based on a study by Mierla et al. (2010), who report an uncertainty in the parameters when different users manually perform GCS reconstruction. For f we set a fixed range from 0.7 – 1.0 (0.1 step size). Thus we get a total of 220 ensemble members for one ELEvoHI event (i.e. 11 values of ϕ , 5 values of λ and 4 values of f). For each ensemble member we select a different sector from the ambient solar wind provided by the WSA/HUX model combination according to the propagation direction, half angle, start- and end-point. In Figure 2, the WSA/HUX model results for event #5 are shown. The white box indicates the area from which the ambient solar wind speed for one individual run of ELEvoHI is computed. Shown is the area for the minimum propagation direction, ϕ_{STA} of 56° with a λ of 50° . For each ensemble member the area surrounded by the white box is slightly

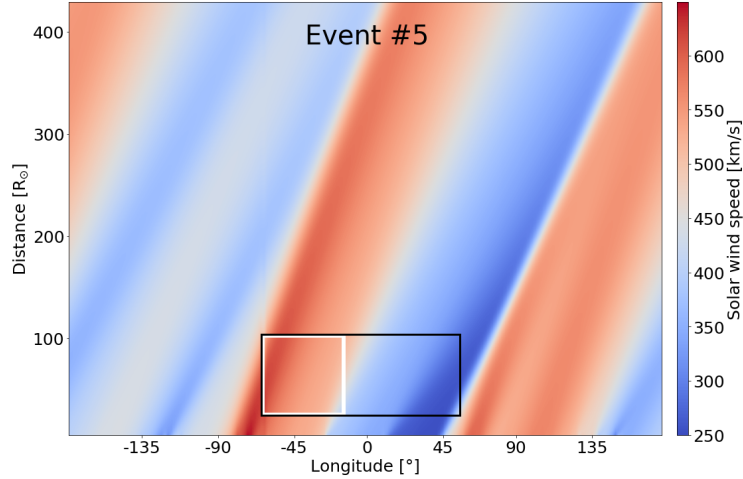


Figure 2: Ambient solar wind speed provided by the WSA/HUX model for event #5. The white box defines the area that is used to calculate an estimate of the ambient solar wind speed for the ensemble member of ELEvoHI corresponding to the minimum propagation direction ($\phi_{STA} = 56^\circ$) with the maximum half width ($\lambda = 50^\circ$). The black box indicates the total area based on all the ensemble members of ELEvoHI for this event. The longitude of 0° corresponds to the longitude of Earth.

305 different according to ϕ and λ . The black box plotted indicates the total area based
 306 on all ELEvoHI ensemble members for this event.

307 Running ELEvoHI in ensemble mode enables us to calculate a mean and a median
 308 predicted CME arrival time and also to define an uncertainty. In addition, we can give
 309 a probability for whether a CME is likely to hit Earth or not. When all of the 220
 310 ensemble members predict an arrival at Earth, we assume the predicted likelihood of
 311 an Earth hit to be 100%.

312 4 Results

313 We perform ELEvoHI ensemble modeling for 12 CMEs between February 2010
 314 to July 2012 (see Table 1) and compare the predicted arrival times based on STA and
 315 STB HI observations with each other. The CMEs propagated close to the ecliptic
 316 plane and showed clear in situ signatures at L1. A prerequisite for the chosen CMEs
 317 was that the CMEs could be tracked unambiguously in both STA and STB HI j-maps.

318 In Table 3, we list the predicted ensemble median arrival times and speeds with
 319 their standard deviation for each CME under study. It further contains the difference
 320 between the predictions from the two vantage points. We find that the predicted
 321 arrival times for STA and STB can deviate by up to 9.5 hrs while the mean difference
 322 is 6.5 hrs. The mean difference in the arrival speed is 63 km s^{-1} , with an exceptionally
 323 large discrepancy of 189 km s^{-1} for event #10.

324 The largest arrival time differences are found for events #2 and #9. The arrival
 325 probability, based on the number of ensemble members that are predicted to hit Earth,
 326 is 79% for event #2 and only 56% for event #9. According to their relatively large
 327 angle of propagation with respect to the Sun-Earth line, the CMEs #2 ($\phi_{Earth} = 22^\circ$,
 328 $HA = 30^\circ$) and #9 ($\phi_{Earth} = 30^\circ$, $HA = 30^\circ$) are considered as "flank hits". In such
 329 cases, ELEvoHI tends to predict the CME arrival time to be later than expected.

Table 3: List of predicted median arrival times (*Date*) and the standard deviation (*SD*) based on STA and STB observations, respectively. *STA - STB* gives the difference between the predicted median arrival times. *v* is the predicted median arrival speed with the standard deviation and $v_{\text{STA-STB}}$ is the difference in arrival speed between STA and STB predictions

Nr.	Date STA	SD _{STA} [h]	Date STB	SD _{STB} [h]	STA - STB [h]	v_{STA} [km s ⁻¹]	v_{STB} [km s ⁻¹]	$v_{\text{STA-STB}}$ [km s ⁻¹]
1	2010-02-07 11:24	1.5	2010-02-07 20:24	2.1	-9.0	455 ± 17	395 ± 11	60
2	2010-03-24 07:17	9.1	2010-03-24 16:40	4.1	-9.5	401 ± 32	351 ± 11	50
3	2010-04-05 13:23	2.5	2010-04-05 16:06	0.4	-2.7	649 ± 37	625 ± 5	24
4	2010-04-11 16:07	0.6	2010-04-12 00:12	5.1	-8.1	443 ± 6	391 ± 33	52
5	2010-05-27 17:36	1.9	2010-05-28 02:26	1.2	-8.8	455 ± 9	407 ± 9	48
6	2010-10-30 11:24	1.4	2010-10-30 04:43	7.1	6.7	432 ± 7	476 ± 45	-44
7	2011-02-04 01:08	2.4	2011-02-03 22:24	7.3	4.5	387 ± 9	446 ± 34	-59
8	2011-02-18 06:22	2.8	2011-02-18 10:34	6.1	-4.3	478 ± 18	407 ± 50	71
9	2011-09-10 18:55	14.9	2011-09-10 09:48	5.4	9.1	396 ± 46	430 ± 18	-34
10	2012-01-24 17:49	4.0	2012-01-24 13:29	3.6	4.3	793 ± 103	982 ± 150	-189
11	2012-06-16 15:47	3.8	2012-06-16 07:53	5.2	7.9	712 ± 72	749 ± 143	-37
12	2012-07-14 22:16	4.9	2012-07-14 18:53	3.7	3.5	658 ± 80	579 ± 28	89

330 The reason may be found in the assumed circular CME front for $f = 1.0$. For future
331 versions of ELEvoHI, we will consider different approaches to tackle such extreme
332 delays for flank encounters.

333 Event #11 occurred on June 14, 2012 and was studied e.g. by Kubicka et al.
334 (2016) who report two preceding CMEs. However, the WSA/HUX model does not
335 provide the ambient solar wind conditions with preceding CMEs included and is there-
336 fore most probably not suitable for interaction events. The events #1, #4, and #5
337 also show large differences in the predicted arrival times based on STA and STB obser-
338 vations. However, these differences are most certainly related to large variance in the
339 modeled ambient solar wind speeds that are used as input to ELEvoHI (see Section 4.2
340 and Figure 5 and 6).

341 4.1 Tracking different parts of the CME front

342 It is important to keep in mind that different parts of the CME front are tracked
343 in STA and STB HI images. This leads to different input conditions to the ELEvo
344 propagation model for STA and STB. ELEvoHI is designed to take HI tracks for the
345 same CME from different viewpoints. Ideally, predictions should give the same CME
346 speed and direction in both cases. One problem is, however, that the CME is not
347 behaving as a single coherent entity, but is instead moving with different speeds at
348 different longitudes (Owens, Lockwood, & Barnard, 2017), which is not incorporated
349 within ELCon nor in any other HI conversion method (e.g. SSE, FP, and HM).

350 Figure 3 presents two snapshots of a movie for event #5, with the ambient
351 solar wind provided by WSA/HUX model combination and the positions of various
352 spacecraft and planets. The elliptical CME fronts from one ensemble member based
353 on STA and STB observations are shown in red and blue, respectively. The green dots
354 indicate the apex direction of those idealized CME fronts. Further, gray lines from

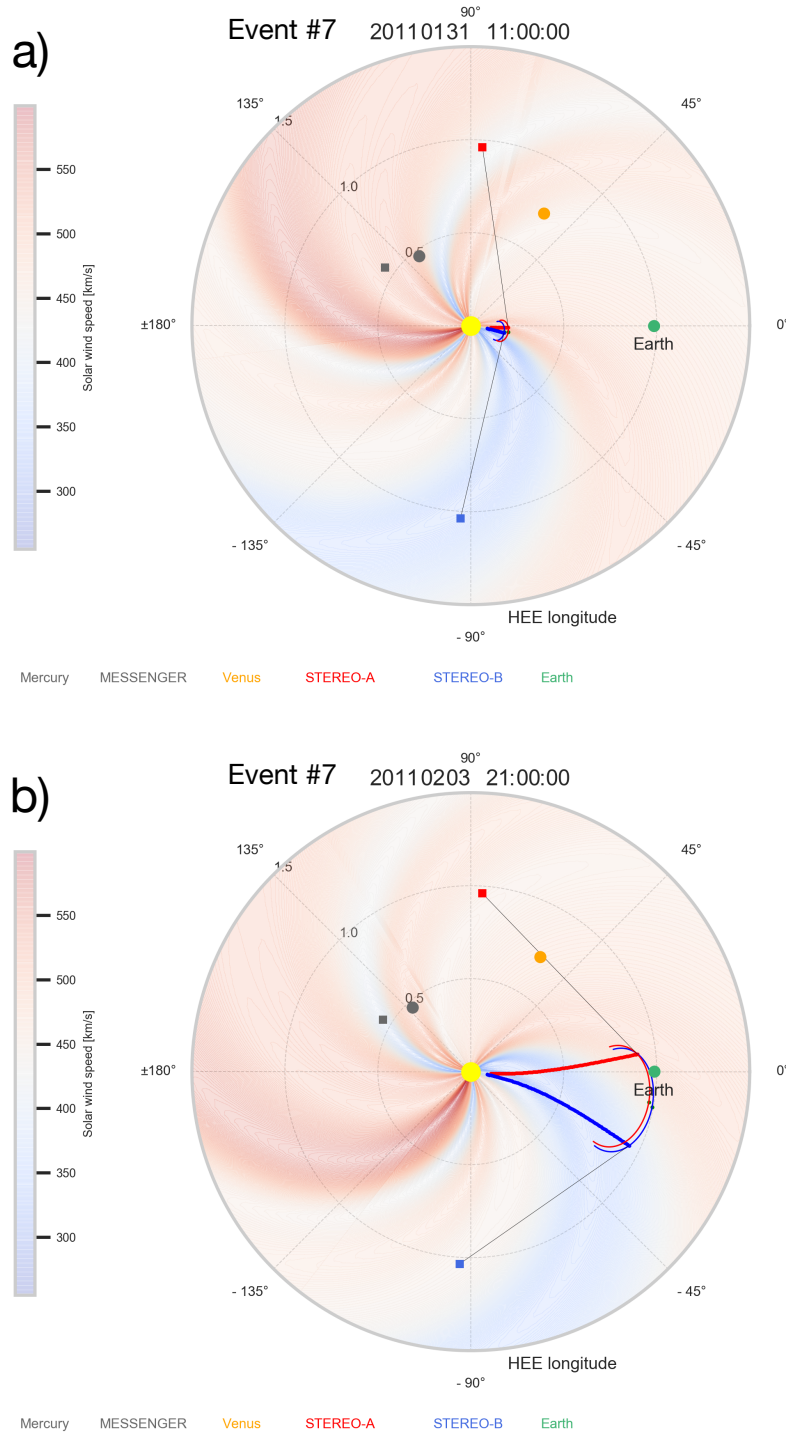


Figure 3: Two snapshots of the CME propagation for one ensemble member based on STA (red) and STB (blue) observations for event #7. The ambient solar wind is computed using the WSA/HUX model combination. The elliptical CME fronts from one ensemble member based on STA and STB observations are shown in red and blue, respectively. The green dots represent the position of the apex of the idealized CME fronts. The curved lines in red and blue show the intercept of the idealized elliptical front of the CME and the tangent (gray lines) for each time step over the course of the simulation for STA and STB, respectively. [Link to the movie.](#)

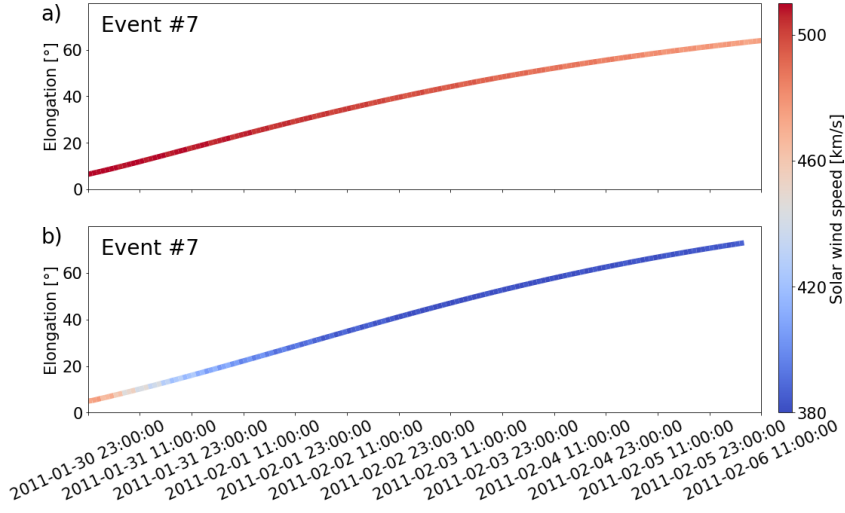


Figure 4: Ambient solar wind speed at the tangent points for event #7. Plotted are time series of the elongation angles of the tangent points as seen from STA (top panel) and STB (bottom panel) colour-coded according to the speed of the ambient solar wind at that tangent point.

355 the two STEREO spacecraft to the elliptical CME fronts are plotted. These tangents
 356 correspond to the elongations of the leading edge of the CME at these times. At the
 357 end of these lines, we add a point, which is the 'tangent point' at each time step. Over
 358 the course of the simulation, these points trace out curved lines, in red and blue for
 359 STA and STB, respectively. From Figure 3, it is obvious that, in the near-Sun part of
 360 the HI FOV, the observed leading edge is close to the apex of the idealized CME front
 361 for both STEREO spacecraft. As the CME propagates, the tangent point, i.e. the part
 362 of the CME with the greatest elongation seen by STA and STB progressively moves
 363 out to the flanks of the ellipse. Based on the observations of these tangent points, the
 364 prediction for the whole front is conducted. Hence, the apex of the CME is, if at all,
 365 only observed for a short period of time. In order to get an estimate of the CME Earth
 366 arrival we have to assume a designated shape of the CME front, which is in our case,
 367 an ellipse. As shown by Owens et al. (2017) this assumption might not be valid since
 368 the CME interacts with the ambient solar wind.

369 4.2 Effect of the ambient solar wind

370 When considering different points along the idealized elliptical CME front, it is
 371 noteworthy that the ambient solar wind speeds at these points would likely be different.
 372 Furthermore, the part of the CME front corresponding to the greatest elongation as
 373 seen by STA and STB (i.e. the points corresponding to the tangent to the CME front)
 374 would propagate in different ambient solar wind conditions. In Figure 4, the modeled
 375 time-elongation profiles of the tangent points seen from STA (top panel) and STB
 376 (bottom panel) are shown.

377 These profiles are obtained from one modeled ensemble member of the ELEvoHI
 378 prediction, separately for STA and STB (see Figure 3), and are therefore available
 379 from 2011-01-30 23:00 until 2011-02-06 11:00. As long as the CME front could be
 380 tracked in HI images (until about 20110202 01:00), the plotted profiles are consistent
 381 with the measured HI time-elongation profiles, obtained using the SATPLOT tool.
 382 The colors represent the speed of the ambient solar wind at the corresponding points.

383 Due to the propagation of the modeled CME in the heliosphere, the elongation of the
 384 tangent point ranges from roughly 6° to about 64° and the speed of the ambient solar
 385 wind at these points ranges from 470 km s^{-1} to 525 km s^{-1} for STA (top panel in
 386 Figure 4). The range of the elongation is slightly larger for STB (5° to 74°) but the
 387 ambient solar wind speed ranges only from $\approx 380 \text{ km s}^{-1}$ to $\approx 480 \text{ km s}^{-1}$.

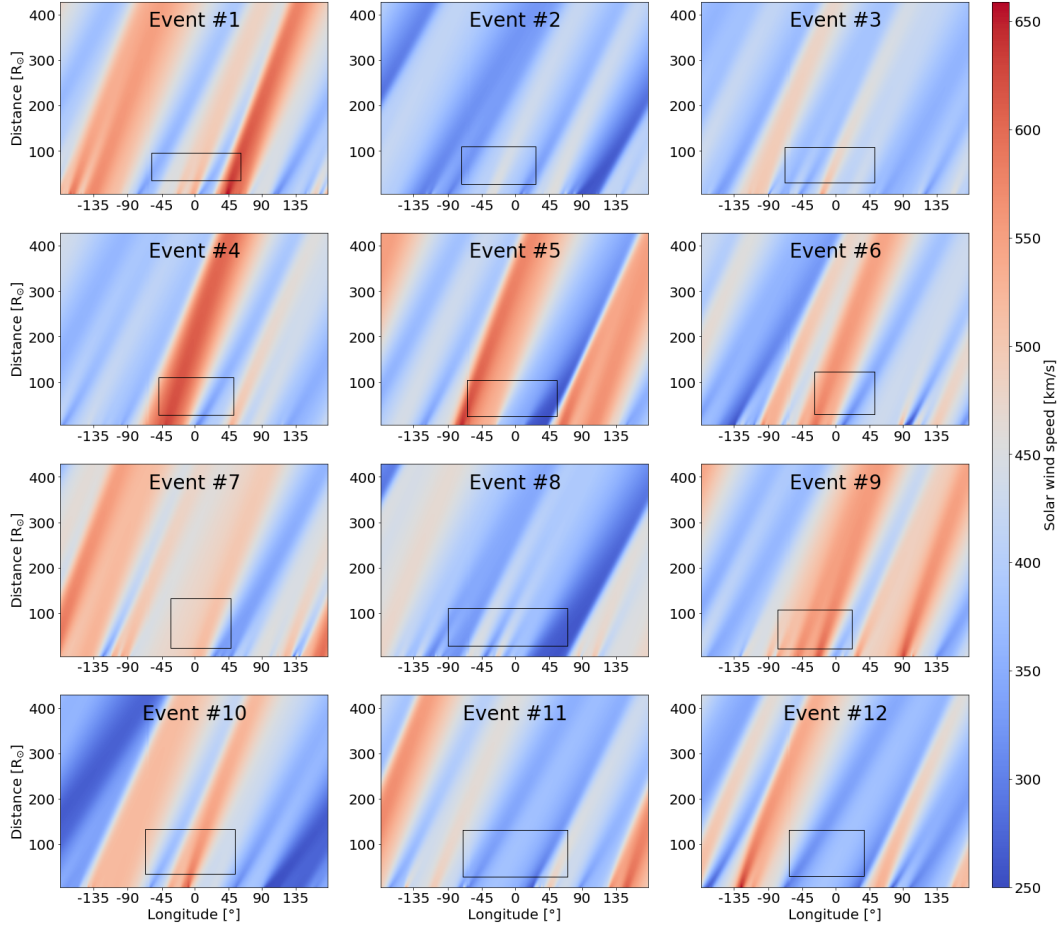


Figure 5: Ambient solar wind speed provided by the WSA/HUX model combination for all 12 events under study. The black boxes define the areas that are used to estimate how structured the ambient solar wind is for each CME. Longitude of 0° corresponds to the longitude of Earth.

388 In the previous paragraph, we considered the ambient solar wind speed at the
 389 tangent point for one ensemble member. Additionally, we examine the distribution of
 390 the ambient solar wind speed considered for all ensemble members (see black boxes in
 391 Figures 2 and 5) that are used as input to ELEvoHI for a single CME. From the areas
 392 framed by the black boxes, we calculate the standard deviation and correlate those to
 393 the absolute values of the difference between STA and STB arrival time predictions
 394 for each event (see Figure 6). This gives us the possibility to check the influence of the
 395 ambient solar wind on the arrival time differences. We obtain a Pearson correlation
 396 coefficient of $cc = 0.52$ for all events under study. However, when excluding events #2
 397 and #9, which are considered as "flank hits", and excluding event #11 (CME-CME
 398 interaction event), the Pearson correlation coefficient increases to $cc = 0.92$. This

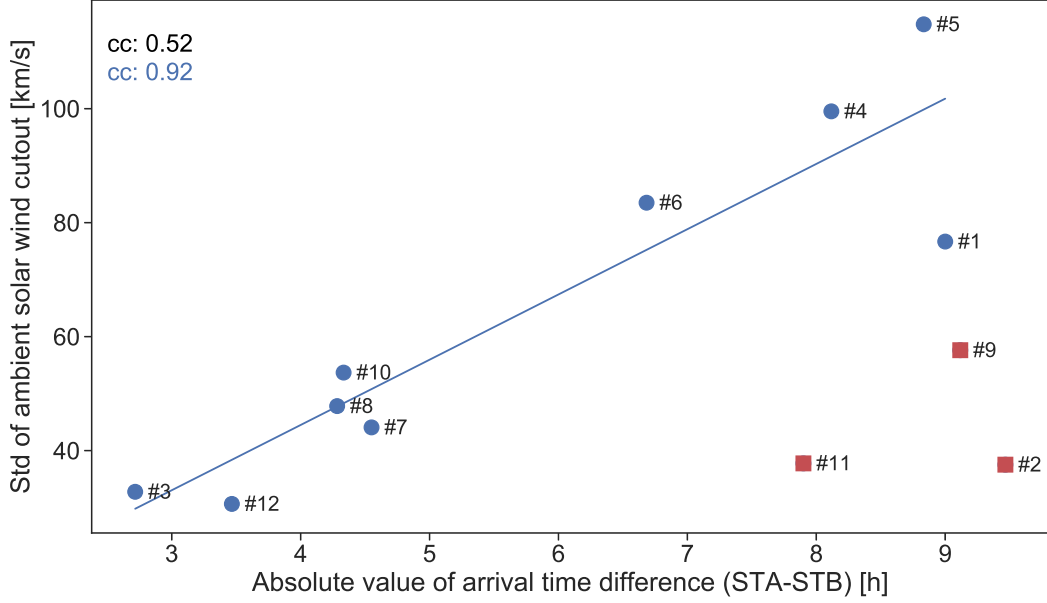


Figure 6: Standard deviation of the ambient solar wind vs. the arrival time difference between STA and STB predictions. The Pearson correlation coefficient for all events under study (black) is calculated. In blue we present the Pearson correlation coefficient and a linear fit when excluding the outliers (indicated by the red boxes), i.e. flank hits (Events #2 and #9) and the CME-CME interaction event (Event #11).

399 indicates that a more structured ambient solar wind (i.e. a larger standard deviation)
 400 leads to a larger differences between STA and STB arrival time prediction.

401 4.3 Comparison to in situ arrivals

402 Figure 7 shows the distributions of the arrival time and arrival speed differences
 403 with respect to the in situ arrivals for all ensemble members for each CME. Blue and
 404 orange correspond to STB and STA ensemble predictions, respectively. The black
 405 horizontal lines indicate the median values of each distribution. When comparing
 406 the median predicted arrival times to the in situ arrivals, we obtain a mean absolute
 407 error (MAE) over all events of 7.5 ± 9.5 hrs and a root mean square error (RMSE) of
 408 ≈ 10.4 hrs. A mean error (ME) of ≈ 4 hrs indicates, in this setup, that ELEvoHI tends
 409 to predict the arrivals too late. The highest arrival time discrepancy is found for event
 410 #9 where the prediction based on STA is 31 hrs too late. When comparing the median
 411 predicted arrival speeds to the in situ speeds we get a MAE of 87 ± 111 km s⁻¹, a
 412 RMSE of ≈ 123 km s⁻¹ and a ME of ≈ 52 km s⁻¹. The highest speed difference is found
 413 for the STB prediction of event #10, overestimating the arrival speed by 369 km s⁻¹.

414 Interestingly, event #10 gives an accurate predicted arrival time, even though the
 415 predicted arrival speed is highly overestimated. When performing GCS reconstruction
 416 we obtain a high latitude and a large tilt angle for this CME meaning that the 3D
 417 propagation direction differs from that in the ecliptic plane (see Table 2). As already
 418 mentioned, event #11 is a CME-CME interaction event which explains the large dis-
 419 crepancy especially for the predicted arrival speed. The reason might be found in an
 420 extremely low drag due to preconditioning in the interplanetary space (Y. D. Liu et
 421 al., 2014; Rollett et al., 2014; Temmer & Nitta, 2015).

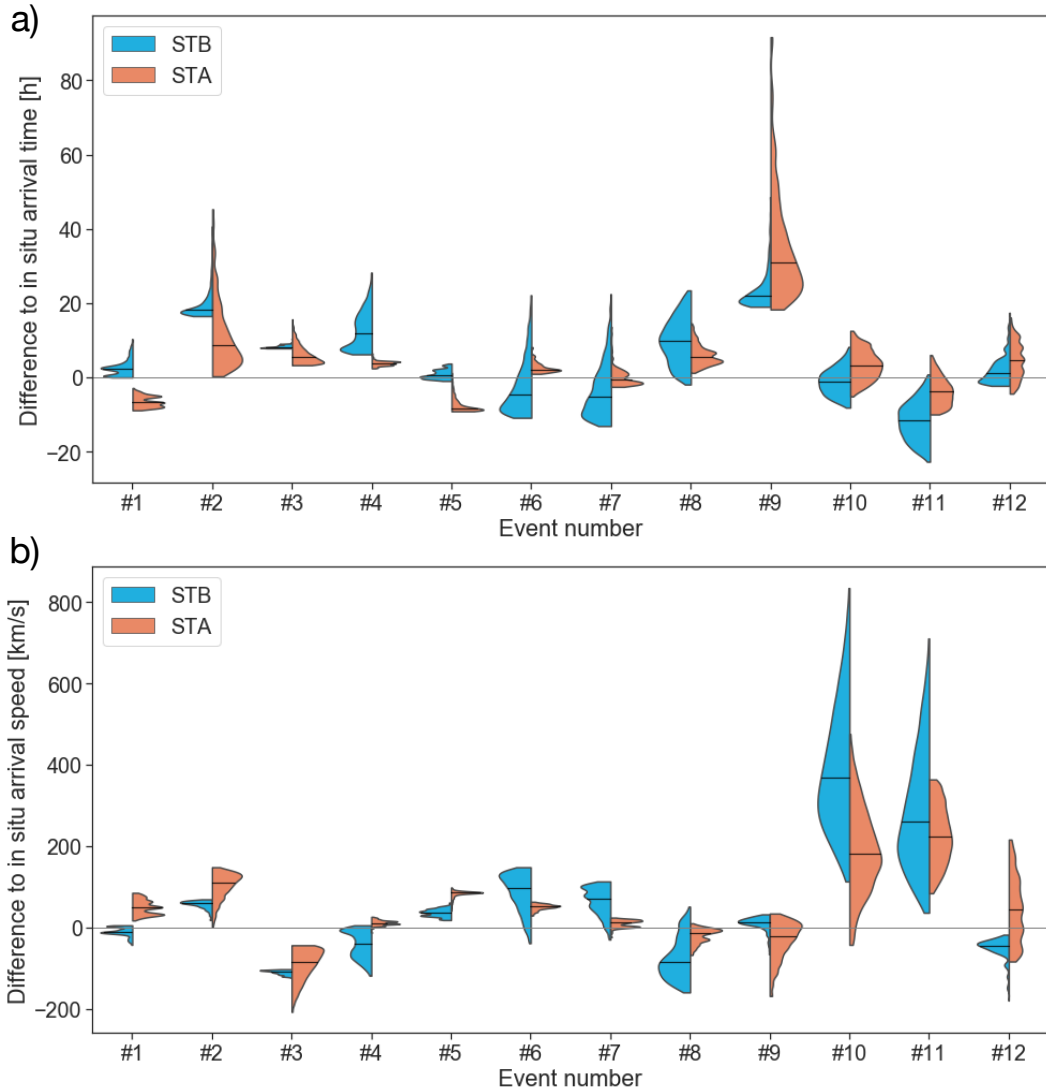


Figure 7: Frequency distributions derived from all ensemble members for the arrival time prediction (top panel) and the arrival speed prediction (bottom panel) based on HI data from STB (blue) and STA (orange), respectively. In the top panel, positive values correspond to a late arrival time prediction while negative values indicate an early arrival prediction. Positive/negative values in the bottom panel indicate an over-/underestimated arrival speed prediction. The black horizontal bars show the median values of the distributions of all the ensemble members for STB and STA.

5 Discussion and Conclusions

We present the ELEvoHI ensemble modeling results for 12 CMEs, occurring between February 2010 and July 2012, that were observed by both STEREO spacecraft. This study mainly focuses on the difference of the modeled arrival time and arrival speed when using STA and STB HI observations, separately. We find on average a difference of 6.5 hrs between arrival time predictions from the two spacecraft but the largest difference is about 9.5 hrs for event #9. For the arrival speed we find a mean difference between STA and STB predictions of 63 km s^{-1} with a maximum difference of 189 km s^{-1} for event #10.

ELEvoHI tends to predict the arrival time later than observed for CMEs that are considered as 'flank hits' (event #2 and event #9). For such events the propagation direction with respect to Earth is larger than 20° , and not all of the ensemble members predict an Earth impact. The reason for the late arrival prediction may be found in the assumed circular shape (for $f = 1.0$) and the highly curved flanks.

We provide two CME arrival time and arrival speed predictions, from STA and STB observation, for the same CME to examine the reasons for the discrepancy between these two predictions. We find, that the CME front propagates in different ambient solar wind conditions when observed in STA and STB HI images. However the kinematics of the CME front obtained e.g. by STA data is used for modeling of the whole CME front, including the Earth-directed part. The same applies for predictions based on STB data, which is the reason for the differences in the predicted arrival times based on STA and STB observations.

We further see, that an ambient solar wind exhibiting a high variance within the area used for ELEvoHI model predictions leads to larger discrepancies between STA and STB model predictions. We obtain a Pearson correlation coefficient ($cc = 0.92$), when excluding flank hits (events #2 and event #9) and the CME-CME interaction event (event #11). Furthermore, we assume that in such cases the CME front is more likely to deform from an idealized elliptical shape due to interaction with the ambient solar wind (Owens et al., 2017; Riley & Crooker, 2004).

The current CME forecasting abilities in the community are summarized in Riley et al. (2018). They analyzed CME forecasts that have been submitted to the Community Coordinated Modeling Center (CCMC) scoreboard from 2013 to mid-2018. The CCMC scoreboard is a platform provided to scientists to compare their forecasts with each other in real-time. Riley et al. (2018) found that the CME shock arrival times for all models combined are predicted on average within ± 10 hrs but with standard deviations of sometimes more than 20 hrs. The best model performance was found for the WSA-ENLIL+Cone model (Odstrcil et al., 2004), run by the UK Met Office, having a bias of 1 hour, a MAE of 13 hrs and a standard deviation of 15 hrs. The results of this study are similar to the findings of Riley et al. (2018) when comparing the modeled arrival times to the actual arrivals of CMEs, as determined from in situ measurements. Here, we only perform hindcasts of CME arrivals. For the 24 arrival predictions (12 based on STA and 12 based on STB observations), we obtain a MAE of 7.5 ± 9.5 hrs, a RMSE of ≈ 10.4 hrs and a ME of ≈ 4 hrs for the arrival time. For the arrival speed, we get a MAE of $87 \pm 111 \text{ km s}^{-1}$, a RMSE of $\approx 123 \text{ km s}^{-1}$ and a ME of $\approx 52 \text{ km s}^{-1}$.

As already mentioned, event #11 is a CME-CME interaction event studied e.g. by Kubicka et al. (2016). This CME was closely preceded by two other CMEs that erupted one and two days before this event and that altered the conditions in the heliosphere. The arrival time prediction for this CME is about 11 hrs too early, while the arrival speed is greatly overestimated (by 260 km s^{-1}) using the ambient solar wind solutions provided by the WSA/HUX model. However, this model does not consider preceding

473 CMEs and is likely not valid in such cases. An additional approach to infer the ambient
474 solar wind conditions in the low heliosphere is shown in Barnard, Owens, Scott, and
475 Jones (2019). In this study the authors established a statistical relationship between
476 the solar wind speed in the low heliosphere and the variability in HI images. A recent
477 study by Amerstorfer et al. (2020) focuses on different input parameters to ELEvoHI
478 including three possible methods to infer the ambient solar wind conditions needed
479 by the model. Their results indicate that the ambient solar wind obtained from the
480 WSA/HUX model provides the best results.

481 ELEvoHI provides ensemble predictions based on various inputs, namely propaga-
482 tion direction, half width, inverse aspect ratio and ambient solar wind speed. In the
483 current version, ELEvoHI is not able to react to possible deflections of a CME during
484 its propagation. Furthermore, the elliptical CME shape, once defined by the input
485 parameters, does not change during propagation. This has been shown to be invalid
486 by, for example, Rollett et al. (2014), who performed a case study by combining HI
487 data with in situ data to ascertain the kinematics of the 2012, March 7 CME. The
488 authors demonstrated evidence for an asymmetric evolution of the CME, which was
489 caused by the preconditioned ambient solar wind resulting in a different drag regime
490 influencing different parts of the CME.

491 Barnard et al. (2017) found that the failure to take into account CME deflection
492 and deformation is an important factor when considering CME propagation in the
493 heliosphere and would likely lead to uncertainties in the arrival time and arrival speed
494 prediction. The authors additionally showed that different tracks lead to quite differ-
495 ent CME arrival time predictions. By using HI observations with better solar wind
496 modeling and varying CME frontal shapes we should be able to improve our current
497 arrival time predictions (Barnard, Owens, Scott, & de Koning, 2020).

498 A number of studies have taken advantage of stereoscopic HI observations, from
499 the two STEREO spacecraft, to glean information on CME propagation and evolution
500 (e.g. Davies et al., 2013; Y. Liu et al., 2010; Lugaz, 2010; Volpes & Bothmer, 2015).
501 We believe, that a stereoscopic view on CMEs incorporated in ELEvoHI will improve
502 the arrival time predictions substantially. Therefore, we strongly support ESA’s L5
503 mission, equipped with a heliospheric imager (Kraft, Puschmann, & Luntama, 2017;
504 Lavraud et al., 2016), and an additional heliospheric imager at L1. Fortunately, the
505 upcoming Earth-orbiting PUNCH mission (launch planned in 2023) will also possess
506 wide-angle white-light heliospheric imagers, as well as a coronagraph, and will be
507 able to provide additional observations of CMEs. Based on information from these
508 additional vantage points, more accurate CME arrival predictions are likely to be
509 achieved. Since ELEvoHI is ready to be used in near real-time, future HI observations
510 are essential for further CME arrival predictions. STA, currently near L5, will have
511 moved beyond L4 by 2027, so it will be necessary to have heliospheric imagers that
512 are observing the space between Sun and Earth after around 2030.

513 In a next step, we want to further develop ELEvoHI in such a way that it can
514 combine HI data from two vantage points in order to constrain the CME and exclude
515 ensemble runs that are not consistent with the observations. Also the CME shape
516 can be constrained by multiple HI observations and therefore, we aim to make the
517 CME front deformable during the propagation through the heliosphere. Hence, the
518 assumed elliptical CME front would be able to adjust according to the ambient solar
519 wind conditions. Scott et al. (2019) showed that ghost fronts in the HI observations
520 can be used to infer the structure of a CME. Using their approach, we also aim to
521 improve our model by verifying and constraining the CME shape.

6 Data Sources

Data

STEREO/HI: <https://www.ukssdc.ac.uk/solar/stereo/data.html>
 STEREO/COR2 and SoHO/LASCO: <https://sdac.virtualsolar.org/cgi/>
 NSO/GONG: <https://gong.nso.edu/data/magmap/>
 HELCATS: <https://www.helcats-fp7.eu>
 ICMECAT: <https://doi.org/10.6084/m9.figshare.6356420>

Model

ELEvoHI is available at <https://zenodo.org/record/3873420>.
 EAGEL is available at <https://zenodo.org/record/4154458>.

Results

The visualization of each prediction result, i.e. movies and figures, can be downloaded from <https://doi.org/10.6084/m9.figshare.12758312.v1>.

Software

IDLTM Version 8.4
 Python 3.7.6
 SATPLOT: https://hesperia.gsfc.nasa.gov/ssw/stereo/secchi/idl/jpl/satplot/SATPLOT_User_Guide.pdf

Acknowledgments

T.A., J.H., M.B., M.A.R., C.M., A.J.W., R.L.B, and U.V.A. thank the Austrian Science Fund (FWF): P31265-N27, J4160-N27, P31659-N27, P31521-N27.

References

- Altschuler, M. D., & Newkirk, G. (1969, September). Magnetic Fields and the Structure of the Solar Corona. I: Methods of Calculating Coronal Fields. *Solar Phys.*, *9*, 131-149. doi: 10.1007/BF00145734
- Amerstorfer, T., Hinterreiter, J., Reiss, M. A., Möstl, C., Davies, J. A., Bailey, R. L., ... Harrison, R. A. (2020, August). CME arrival prediction using ensemble modeling based on heliospheric imaging observations. *arXiv e-prints*, arXiv:2008.02576.
- Amerstorfer, T., Möstl, C., Hess, P., Temmer, M., Mays, M. L., Reiss, M. A., ... Bourdin, P. A. (2018, July). Ensemble Prediction of a Halo Coronal Mass Ejection Using Heliospheric Imagers. *Space Weather*, *16*(7), 784-801. doi: 10.1029/2017SW001786
- Arge, C. N., Odstrcil, D., Pizzo, V. J., & Mayer, L. R. (2003, September). Improved Method for Specifying Solar Wind Speed Near the Sun. In M. Velli, R. Bruno, F. Malara, & B. Bucci (Eds.), *Solar wind ten* (Vol. 679, p. 190-193). doi: 10.1063/1.1618574
- Barnard, L., Owens, M. J., Scott, C. J., & de Koning, C. A. (2020). Ensemble cme modeling constrained by heliospheric imager observations. *AGU Advances*, *1*(3), e2020AV000214. Retrieved from <https://agupubs.onlinelibrary.wiley.com/doi/abs/10.1029/2020AV000214> (e2020AV000214 10.1029/2020AV000214) doi: 10.1029/2020AV000214
- Barnard, L. A., de Koning, C. A., Scott, C. J., Owens, M. J., Wilkinson, J., & Davies, J. A. (2017, June). Testing the current paradigm for space weather prediction with heliospheric imagers. *Space Weather*, *15*(6), 782-803. doi: 10.1002/2017SW001609
- Barnard, L. A., Owens, M. J., Scott, C. J., & Jones, S. R. (2019, June). Extracting Inner-Heliosphere Solar Wind Speed Information From Heliospheric Imager Observations. *Space Weather*, *17*(6), 925-938. doi: 10.1029/2019SW002226

- 571 Barnes, D., Davies, J. A., Harrison, R. A., Byrne, J. P., Perry, C. H., Bothmer, V.,
 572 ... Odstrcil, D. (2020, June). CMEs in the Heliosphere: III. A Statistical
 573 Analysis of the Kinematic Properties Derived from Stereoscopic Geometrical
 574 Modelling Techniques Applied to CMEs Detected in the Heliosphere from 2008
 575 to 2014 by STEREO/HI-1. *arXiv e-prints*, arXiv:2006.14879.
- 576 Brueckner, G. E., Howard, R. A., Koomen, M. J., Korendyke, C. M., Michels,
 577 D. J., Moses, J. D., ... Eyles, C. J. (1995, December). The Large Angle
 578 Spectroscopic Coronagraph (LASCO). *Solar Phys.*, *162*(1-2), 357-402. doi:
 579 10.1007/BF00733434
- 580 Cannon, P. S. (2013, April). Extreme Space Weather—A Report Published by the
 581 UK Royal Academy of Engineering. *Space Weather*, *11*(4), 138-139. doi: 10
 582 .1002/swe.20032
- 583 Davies, J. A., Harrison, R. A., Perry, C. H., Möstl, C., Lugaz, N., Rollett, T., ...
 584 Savani, N. P. (2012, May). A Self-similar Expansion Model for Use in So-
 585 lar Wind Transient Propagation Studies. *Astrophys. J.*, *750*(1), 23. doi:
 586 10.1088/0004-637X/750/1/23
- 587 Davies, J. A., Harrison, R. A., Rouillard, A. P., Sheeley, N. R., Perry, C. H., Bew-
 588 sher, D., ... Brown, D. S. (2009, January). A synoptic view of solar transient
 589 evolution in the inner heliosphere using the Heliospheric Imagers on STEREO.
 590 *Geophys. Res. Lett.*, *36*(2), L02102. doi: 10.1029/2008GL036182
- 591 Davies, J. A., Perry, C. H., Trines, R. M. G. M., Harrison, R. A., Lugaz, N., Möstl,
 592 C., ... Steed, K. (2013, November). Establishing a Stereoscopic Technique
 593 for Determining the Kinematic Properties of Solar Wind Transients based on
 594 a Generalized Self-similarly Expanding Circular Geometry. *Astrophys. J.*,
 595 *777*(2), 167. doi: 10.1088/0004-637X/777/2/167
- 596 Dumbović, M., Čalogović, J., Vršnak, B., Temmer, M., Mays, M. L., Veronig, A., &
 597 Piantšitsch, I. (2018, February). The Drag-based Ensemble Model (DBEM)
 598 for Coronal Mass Ejection Propagation. *Astrophys. J.*, *854*(2), 180. doi:
 599 10.3847/1538-4357/aaa66
- 600 Eyles, C. J., Harrison, R. A., Davis, C. J., Waltham, N. R., Shaughnessy, B. M.,
 601 Mapson-Menard, H. C. A., ... Rochus, P. (2009, February). The Heliospheric
 602 Imagers Onboard the STEREO Mission. *Solar Phys.*, *254*(2), 387-445. doi:
 603 10.1007/s11207-008-9299-0
- 604 Gopalswamy, N., Lara, A., Lepping, R. P., Kaiser, M. L., Berdichevsky, D., & St.
 605 Cyr, O. C. (2000, January). Interplanetary acceleration of coronal mass
 606 ejections. *Geophys. Res. Lett.*, *27*(2), 145-148. doi: 10.1029/1999GL003639
- 607 Gosling, J. T., Bame, S. J., McComas, D. J., & Phillips, J. L. (1990, June). Coronal
 608 mass ejections and large geomagnetic storms. *Geophys. Res. Lett.*, *17*(7), 901-
 609 904. doi: 10.1029/GL017i007p00901
- 610 Harrison, R. A., Davies, J. A., Barnes, D., Byrne, J. P., Perry, C. H., Bothmer, V.,
 611 ... Odstrčil, D. (2018, April). CMEs in the Heliosphere: I. A Statistical
 612 Analysis of the Observational Properties of CMEs Detected in the Helio-
 613 sphere from 2007 to 2017 by STEREO/HI-1. *Solar Phys.*, *293*(5), 77. doi:
 614 10.1007/s11207-018-1297-2
- 615 Howard, R. A., Moses, J. D., Vourlidas, A., Newmark, J. S., Socker, D. G., Plun-
 616 kett, S. P., ... Carter, T. (2008, April). Sun Earth Connection Coronal and
 617 Heliospheric Investigation (SECCHI). *Space Sci. Rev.*, *136*(1-4), 67-115. doi:
 618 10.1007/s11214-008-9341-4
- 619 Hundhausen, A. J., Stanger, A. L., & Serbicki, S. A. (1994, December). Mass
 620 and energy contents of coronal mass ejections: SMM results from 1980 and
 621 1984-1988. In J. J. Hunt (Ed.), *Solar dynamic phenomena and solar wind*
 622 *consequences, the third soho workshop* (Vol. 373, p. 409).
- 623 Kaiser, M. L., Kucera, T. A., Davila, J. M., St. Cyr, O. C., Guhathakurta, M., &
 624 Christian, E. (2008, April). The STEREO Mission: An Introduction. *Space*
 625 *Sci. Rev.*, *136*(1-4), 5-16. doi: 10.1007/s11214-007-9277-0

- 626 Kay, C., Mays, M. L., & Verbeke, C. (2020, January). Identifying Critical Input
627 Parameters for Improving Drag-Based CME Arrival Time Predictions. *Space*
628 *Weather*, *18*(1), e02382. doi: 10.1029/2019SW002382
- 629 Kay, C., & Opher, M. (2015, October). The Heliocentric Distance where the De-
630 flections and Rotations of Solar Coronal Mass Ejections Occur. *Astrophys. J. Lett.*,
631 *811*(2), L36. doi: 10.1088/2041-8205/811/2/L36
- 632 Kilpua, E. K. J., Jian, L. K., Li, Y., Luhmann, J. G., & Russell, C. T. (2012,
633 November). Observations of ICMEs and ICME-like Solar Wind Structures
634 from 2007 - 2010 Using Near-Earth and STEREO Observations. *Solar Phys.*,
635 *281*(1), 391-409. doi: 10.1007/s11207-012-9957-0
- 636 Kraft, S., Puschmann, K. G., & Luntama, J. P. (2017). Remote sensing opti-
637 cal instrumentation for enhanced space weather monitoring from the L1 and
638 L5 Lagrange points. In B. Cugny, N. Karafolas, & Z. Sodnik (Eds.), *In-*
639 *ternational conference on space optics — ics0 2016* (Vol. 10562, pp. 115 –
640 123). SPIE. Retrieved from <https://doi.org/10.1117/12.2296100> doi:
641 10.1117/12.2296100
- 642 Kubicka, M., Möstl, C., Amerstorfer, T., Boakes, P. D., Feng, L., Eastwood, J. P., &
643 Törmänen, O. (2016, December). Prediction of Geomagnetic Storm Strength
644 from Inner Heliospheric In Situ Observations. *Astrophys. J.*, *833*(2), 255. doi:
645 10.3847/1538-4357/833/2/255
- 646 Lavraud, B., Liu, Y., Segura, K., He, J., Qin, G., Temmer, M., ... Fernández,
647 J. G. (2016, August). A small mission concept to the Sun-Earth La-
648 grangian L5 point for innovative solar, heliospheric and space weather science.
649 *Journal of Atmospheric and Solar-Terrestrial Physics*, *146*, 171-185. doi:
650 10.1016/j.jastp.2016.06.004
- 651 Liu, Y., Davies, J. A., Luhmann, J. G., Vourlidas, A., Bale, S. D., & Lin, R. P.
652 (2010, February). Geometric Triangulation of Imaging Observations to Track
653 Coronal Mass Ejections Continuously Out to 1 AU. *Astrophys. J. Lett.*,
654 *710*(1), L82-L87. doi: 10.1088/2041-8205/710/1/L82
- 655 Liu, Y. D., Luhmann, J. G., Kajdič, P., Kilpua, E. K. J., Lugaz, N., Nitta, N. V., ...
656 Galvin, A. B. (2014, March). Observations of an extreme storm in interplan-
657 etary space caused by successive coronal mass ejections. *Nature Communica-*
658 *tions*, *5*, 3481. doi: 10.1038/ncomms4481
- 659 Lugaz, N. (2010, December). Accuracy and Limitations of Fitting and Stereo-
660 scopic Methods to Determine the Direction of Coronal Mass Ejections from
661 Heliospheric Imagers Observations. *Solar Phys.*, *267*(2), 411-429. doi:
662 10.1007/s11207-010-9654-9
- 663 Lugaz, N., Farrugia, C. J., Davies, J. A., Möstl, C., Davis, C. J., Roussev, I. I.,
664 & Temmer, M. (2012, November). The Deflection of the Two Interacting
665 Coronal Mass Ejections of 2010 May 23-24 as Revealed by Combined In Situ
666 Measurements and Heliospheric Imaging. *Astrophys. J.*, *759*(1), 68. doi:
667 10.1088/0004-637X/759/1/68
- 668 Lugaz, N., Hernandez-Charpak, J. N., Roussev, I. I., Davis, C. J., Vourlidas, A.,
669 & Davies, J. A. (2010, May). Determining the Azimuthal Properties
670 of Coronal Mass Ejections from Multi-Spacecraft Remote-Sensing Obser-
671 vations with STEREO SECCHI. *Astrophys. J.*, *715*(1), 493-499. doi:
672 10.1088/0004-637X/715/1/493
- 673 Luhmann, J. G., Curtis, D. W., Schroeder, P., McCauley, J., Lin, R. P., Larson,
674 D. E., ... Gosling, J. T. (2008, April). STEREO IMPACT Investigation
675 Goals, Measurements, and Data Products Overview. *Space Sci. Rev.*, *136*(1-
676 4), 117-184. doi: 10.1007/s11214-007-9170-x
- 677 Manoharan, P. K., Gopalswamy, N., Yashiro, S., Lara, A., Michalek, G., & Howard,
678 R. A. (2004, June). Influence of coronal mass ejection interaction on propaga-
679 tion of interplanetary shocks. *Journal of Geophysical Research (Space Physics)*,
680 *109*(A6), A06109. doi: 10.1029/2003JA010300

- 681 Manoharan, P. K., & Mujiber Rahman, A. (2011, April). Coronal mass ejec-
 682 tions—Propagation time and associated internal energy. *Journal of At-*
 683 *mospheric and Solar-Terrestrial Physics*, *73*(5-6), 671-677. doi: 10.1016/
 684 j.jastp.2011.01.017
- 685 Mierla, M., Inhester, B., Antunes, A., Boursier, Y., Byrne, J. P., Colaninno, R., ...
 686 Zhukov, A. N. (2010, January). On the 3-D reconstruction of Coronal Mass
 687 Ejections using coronagraph data. *Annales Geophysicae*, *28*(1), 203-215. doi:
 688 10.5194/angeo-28-203-2010
- 689 Möstl, C., & Davies, J. A. (2013, July). Speeds and Arrival Times of Solar Tran-
 690 sients Approximated by Self-similar Expanding Circular Fronts. *Solar Phys.*,
 691 *285*(1-2), 411-423. doi: 10.1007/s11207-012-9978-8
- 692 Möstl, C., Isavnin, A., Boakes, P. D., Kilpua, E. K. J., Davies, J. A., Harrison,
 693 R. A., ... Zhang, T. L. (2017, July). Modeling observations of solar coronal
 694 mass ejections with heliospheric imagers verified with the Heliophysics System
 695 Observatory. *Space Weather*, *15*(7), 955-970. doi: 10.1002/2017SW001614
- 696 Möstl, C., Rollett, T., Frahm, R. A., Liu, Y. D., Long, D. M., Colaninno, R. C., ...
 697 Vršnak, B. (2015, May). Strong coronal channelling and interplanetary evolu-
 698 tion of a solar storm up to Earth and Mars. *Nature Communications*, *6*, 7135.
 699 doi: 10.1038/ncomms8135
- 700 Möstl, C., Rollett, T., Lugaz, N., Farrugia, C. J., Davies, J. A., Temmer, M., ...
 701 Biernat, H. K. (2011, November). Arrival Time Calculation for Interplanetary
 702 Coronal Mass Ejections with Circular Fronts and Application to STEREO Ob-
 703 servations of the 2009 February 13 Eruption. *Astrophys. J.*, *741*(1), 34. doi:
 704 10.1088/0004-637X/741/1/34
- 705 Möstl, C., Weiss, A. J., Bailey, R. L., Reiss, M. A., Amerstorfer, U. V., Amerstor-
 706 fer, T., ... Stansby, D. (2020, July). Prediction of the in situ coronal mass
 707 ejection rate for solar cycle 25: Implications for Parker Solar Probe in situ
 708 observations. *arXiv e-prints*, arXiv:2007.14743.
- 709 Nieves-Chinchilla, T., Vourlidas, A., Raymond, J. C., Linton, M. G., Al-haddad, N.,
 710 Savani, N. P., ... Hidalgo, M. A. (2018, February). Understanding the Internal
 711 Magnetic Field Configurations of ICMEs Using More than 20 Years of Wind
 712 Observations. *Solar Phys.*, *293*(2), 25. doi: 10.1007/s11207-018-1247-z
- 713 Odstreil, D., Pizzo, V. J., Linker, J. A., Riley, P., Lionello, R., & Mikic, Z. (2004,
 714 October). Initial coupling of coronal and heliospheric numerical magnetohy-
 715 drodynamic codes. *Journal of Atmospheric and Solar-Terrestrial Physics*,
 716 *66*(15-16), 1311-1320. doi: 10.1016/j.jastp.2004.04.007
- 717 Owens, M. J., Lockwood, M., & Barnard, L. A. (2017, June). Coronal mass ejections
 718 are not coherent magnetohydrodynamic structures. *Scientific Reports*, *7*, 4152.
 719 doi: 10.1038/s41598-017-04546-3
- 720 Owens, M. J., Lockwood, M., & Barnard, L. A. (2020). The value of cme ar-
 721 rival time forecasts for space weather mitigation. *Space Weather*, *18*(9),
 722 e2020SW002507. Retrieved from [https://agupubs.onlinelibrary](https://agupubs.onlinelibrary.wiley.com/doi/abs/10.1029/2020SW002507)
 723 [.wiley.com/doi/abs/10.1029/2020SW002507](https://agupubs.onlinelibrary.wiley.com/doi/abs/10.1029/2020SW002507) (e2020SW002507
 724 10.1029/2020SW002507) doi: 10.1029/2020SW002507
- 725 Owens, M. J., & Riley, P. (2017, November). Probabilistic Solar Wind Forecast-
 726 ing Using Large Ensembles of Near-Sun Conditions With a Simple One-
 727 Dimensional “Upwind” Scheme. *Space Weather*, *15*(11), 1461-1474. doi:
 728 10.1002/2017SW001679
- 729 Paouris, E., & Mavromichalaki, H. (2017, December). Effective Acceleration Model
 730 for the Arrival Time of Interplanetary Shocks driven by Coronal Mass Ejec-
 731 tions. *Solar Phys.*, *292*(12), 180. doi: 10.1007/s11207-017-1212-2
- 732 Pomoell, J., & Poedts, S. (2018, June). EUHFORIA: European heliospheric forecast-
 733 ing information asset. *Journal of Space Weather and Space Climate*, *8*, A35.
 734 doi: 10.1051/swsc/2018020
- 735 Reiss, M. A., MacNeice, P. J., Mays, L. M., Arge, C. N., Möstl, C., Nikolic, L., &

- 736 Amerstorfer, T. (2019, February). Forecasting the Ambient Solar Wind with
 737 Numerical Models. I. On the Implementation of an Operational Framework.
 738 *Astrophys. J. Suppl. S.*, *240*, 35. doi: 10.3847/1538-4365/aaf8b3
- 739 Reiss, M. A., MacNeice, P. J., Muglach, K., Arge, C. N., Möstl, C., Riley, P.,
 740 ... Amerstorfer, U. (2020, March). Forecasting the Ambient Solar Wind
 741 with Numerical Models. II. An Adaptive Prediction System for Specify-
 742 ing Solar Wind Speed near the Sun. *Astrophys. J.*, *891*(2), 165. doi:
 743 10.3847/1538-4357/ab78a0
- 744 Richardson, I. G., & Cane, H. V. (2010, Jun). Near-Earth Interplanetary Coronal
 745 Mass Ejections During Solar Cycle 23 (1996 - 2009): Catalog and Summary of
 746 Properties. *Solar Phys.*, *264*(1), 189-237. doi: 10.1007/s11207-010-9568-6
- 747 Richardson, I. G., & Cane, H. V. (2012, May). Near-earth solar wind flows and
 748 related geomagnetic activity during more than four solar cycles (1963-2011).
 749 *Journal of Space Weather and Space Climate*, *2*, A02. doi: 10.1051/swsc/
 750 2012003
- 751 Riley, P., & Crooker, N. U. (2004, January). Kinematic Treatment of Coronal Mass
 752 Ejection Evolution in the Solar Wind. *Astrophys. J.*, *600*(2), 1035-1042. doi:
 753 10.1086/379974
- 754 Riley, P., & Lionello, R. (2011, June). Mapping Solar Wind Streams from the Sun
 755 to 1 AU: A Comparison of Techniques. *Solar Phys.*, *270*, 575-592. doi: 10
 756 .1007/s11207-011-9766-x
- 757 Riley, P., Mays, M. L., Andries, J., Amerstorfer, T., Biesecker, D., Delouille, V., ...
 758 Zhao, X. (2018, September). Forecasting the Arrival Time of Coronal Mass
 759 Ejections: Analysis of the CCMC CME Scoreboard. *Space Weather*, *16*(9),
 760 1245-1260. doi: 10.1029/2018SW001962
- 761 Rollett, T., Möstl, C., Isavnin, A., Davies, J. A., Kubicka, M., Amerstorfer, U. V.,
 762 & Harrison, R. A. (2016, Jun). EIEvoHI: A Novel CME Prediction Tool for
 763 Heliospheric Imaging Combining an Elliptical Front with Drag-based Model
 764 Fitting. *Astrophys. J.*, *824*(2), 131. doi: 10.3847/0004-637X/824/2/131
- 765 Rollett, T., Möstl, C., Temmer, M., Frahm, R. A., Davies, J. A., Veronig, A. M., ...
 766 Zhang, T. L. (2014, July). Combined Multipoint Remote and in situ Obser-
 767 vations of the Asymmetric Evolution of a Fast Solar Coronal Mass Ejection.
 768 *Astrophys. J. Lett.*, *790*(1), L6. doi: 10.1088/2041-8205/790/1/L6
- 769 Rouillard, A. P., Davies, J. A., Forsyth, R. J., Rees, A., Davis, C. J., Harrison,
 770 R. A., ... Perry, C. H. (2008, May). First imaging of corotating interaction
 771 regions using the STEREO spacecraft. *Geophys. Res. Lett.*, *35*(10), L10110.
 772 doi: 10.1029/2008GL033767
- 773 Ruffenach, A., Lavraud, B., Farrugia, C. J., Démoulin, P., Dasso, S., Owens, M. J.,
 774 ... Galvin, A. B. (2015, January). Statistical study of magnetic cloud erosion
 775 by magnetic reconnection. *Journal of Geophysical Research (Space Physics)*,
 776 *120*(1), 43-60. doi: 10.1002/2014JA020628
- 777 Savani, N. P., Owens, M. J., Rouillard, A. P., Forsyth, R. J., & Davies, J. A. (2010,
 778 May). Observational Evidence of a Coronal Mass Ejection Distortion Directly
 779 Attributable to a Structured Solar Wind. *Astrophys. J. Lett.*, *714*(1), L128-
 780 L132. doi: 10.1088/2041-8205/714/1/L128
- 781 Schatten, K. H. (1971). Current sheet magnetic model for the solar corona. *Cosmic*
 782 *Electrodynamics*, *2*, 232-245.
- 783 Schatten, K. H., Wilcox, J. M., & Ness, N. F. (1969, March). A model of inter-
 784 planetary and coronal magnetic fields. *Solar Phys.*, *6*, 442-455. doi: 10.1007/
 785 BF00146478
- 786 Scott, C. J., Owens, M. J., de Koning, C. A., Barnard, L. A., Jones, S. R., &
 787 Wilkinson, J. (2019, April). Using Ghost Fronts Within STEREO Heliospheric
 788 Imager Data to Infer the Evolution in Longitudinal Structure of a Coronal
 789 Mass Ejection. *Space Weather*, *17*(4), 539-552. doi: 10.1029/2018SW002093
- 790 Sheeley, N. R., Walters, J. H., Wang, Y. M., & Howard, R. A. (1999, November).

- 791 Continuous tracking of coronal outflows: Two kinds of coronal mass ejections.
792 *J. Geophys. Res.*, *104*(A11), 24739-24768. doi: 10.1029/1999JA900308
- 793 Srivastava, N., & Venkatakrisnan, P. (2004, October). Solar and interplanetary
794 sources of major geomagnetic storms during 1996-2002. *Journal of Geophysical*
795 *Research (Space Physics)*, *109*(A10), A10103. doi: 10.1029/2003JA010175
- 796 Temmer, M., & Nitta, N. V. (2015, March). Interplanetary Propagation Behavior of
797 the Fast Coronal Mass Ejection on 23 July 2012. *Solar Phys.*, *290*(3), 919-932.
798 doi: 10.1007/s11207-014-0642-3
- 799 Thernisien, A., Vourlidas, A., & Howard, R. A. (2009, May). Forward Modeling of
800 Coronal Mass Ejections Using STEREO/SECCHI Data. *Solar Phys.*, *256*(1-2),
801 111-130. doi: 10.1007/s11207-009-9346-5
- 802 Thernisien, A. F. R., Howard, R. A., & Vourlidas, A. (2006, Nov). Modeling of Flux
803 Rope Coronal Mass Ejections. *Astrophys. J.*, *652*(1), 763-773. doi: 10.1086/
804 508254
- 805 Volpes, L., & Bothmer, V. (2015, October). An Application of the Stereoscopic
806 Self-similar-Expansion Model to the Determination of CME-Driven Shock
807 Parameters. *Solar Phys.*, *290*(10), 3005-3022. doi: 10.1007/s11207-015-0775-z
- 808 Vršnak, B., Žic, T., Vrbanec, D., Temmer, M., Rollett, T., Möstl, C., ... Shan-
809 mugaraju, A. (2013, July). Propagation of Interplanetary Coronal Mass
810 Ejections: The Drag-Based Model. *Solar Phys.*, *285*(1-2), 295-315. doi:
811 10.1007/s11207-012-0035-4
- 812 Žic, T., Vršnak, B., & Temmer, M. (2015, June). Heliospheric Propagation of
813 Coronal Mass Ejections: Drag-based Model Fitting. *Astrophys. J. Suppl. S.*,
814 *218*(2), 32. doi: 10.1088/0067-0049/218/2/32
- 815 Wang, Y.-M., & Sheeley, N. R., Jr. (1995, July). Solar Implications of ULYSSES
816 Interplanetary Field Measurements. *Astrophys. J. Lett.*, *447*, L143. doi: 10
817 .1086/309578
- 818 Zuccarello, F. P., Bemporad, A., Jacobs, C., Mierla, M., Poedts, S., & Zuccarello,
819 F. (2012, January). The Role of Streamers in the Deflection of Coronal
820 Mass Ejections: Comparison between STEREO Three-dimensional Recon-
821 structions and Numerical Simulations. *Astrophys. J.*, *744*(1), 66. doi:
822 10.1088/0004-637X/744/1/66